Instability threshold in a large balanced magneto-optical trap

M. Gaudesius, R. Kaiser, and G. Labeyrie[*]

Université Côte d'Azur, CNRS, Institut de Physique de Nice, 06560 Valbonne, France

Y.-C. Zhang and T. Pohl

Department of Physics and Astronomy, Aarhus University, DK 8000 Aarhus, Denmark

Large clouds of cold atoms prepared in a magneto-optical trap can develop spatiotemporal instabilities when the frequency of the trapping lasers is brought close to the atomic resonance. This system bears close similarities with trapped plasmas, whereby effective Coulomb interactions are induced by the exchange of scattered photons and lead to collective nonlinear dynamics of the trapped atoms. We report in this paper a detailed experimental study of the instability threshold, and comparisons with three-dimensional simulations of the interacting, laser-driven cloud.

I. INTRODUCTION

The magneto-optical trap (MOT), first demonstrated in 1987 [1], is widely used nowadays. It has triggered a broad field of research in the past decades. Following its initial demonstration, early work explored the role of sub-Doppler mechanisms [2] and multiple scattering of light [3]. In addition to representing essential experimental technology to reach quantum degeneracy in ultracold gases, MOTs can harbor in the large atom number limit a variety of interesting nonlinear phenomena that are not yet fully understood and bear intriguing ties to plasma [4–8] and stellar physics [9,10]. Descriptions borrowed from the fields of nonlinear dynamics [11,12] and fluid physics [13] have been employed to investigate these phenomena.

In a MOT with a large number of trapped atoms N, these are subjected to three forces. A trapping and cooling force is exerted by laser beams in the presence of a magnetic field gradient. This force depends on laser and magnetic field parameters, but not on N. Two additional, *collective* forces appear when N is large enough. First, the laser beams are attenuated inside the atom cloud due to photon scattering. This attenuation yields a compressive correction to the trapping force [14]. Second, the scattered photons can be rescattered by other atoms, which gives rise to a Coulomb-like repulsive force [3]. It is the interplay between these three forces that can generate unstable dynamics in large MOTs.

During the last two decades, instabilities in MOTs have been studied in various configurations [9,11,12,15,16]. In Ref. [9] we reported an unstable behavior for a large balanced MOT (see Sec. II) and presented a preliminary study of its instability threshold. A simple unidimensional analytical model allowed us to provide a rough instability criterion. In the present work we provide a detailed analysis of the instability threshold using an improved experimental scheme where the number of trapped atoms is controlled. Some of our observations deviate from the scaling predicted by the analytical model of Ref. [9]. We thus developed a three-dimensional numerical simulation based on microscopic theoretical ingredients, whose results are in qualitative agreement with the experiment.

The article is organized as follows. In Sec. II we describe our experimental setup and measurement procedure. We then review previous theoretical models of MOT instabilities in Sec. III A, and describe our numerical approach in Sec. III B. In Sec. IV we present our experimental results and discuss the comparison to our numerical simulations. The implications of our findings and ensuing perspectives for future work are outlined in Secs. V and VI.

II. EXPERIMENTAL SETUP

Our large MOT and its characteristics have been thoroughly described in Ref. [17]. Here we briefly reiterate the aspects that are most relevant to the present work.

We use six large (3.4 cm waist) trapping laser beams of same intensity tuned close (detuning δ) to the $F = 2 \rightarrow F' = 3$ transition of the ^{87}Rb $D2$ line to trap and cool atoms from an ambient vapor (see Fig. 1). These six beams, originating from the same source coupled into single-mode optical fibers, form three counterpropagating pairs crossing at 90°. Because of this balanced arrangement, the nature of the instabilities is different from that of Refs. [11,16] where the beams were retroreflected, such that the center-of-mass motion played a dominant role in the nonlinear dynamics of the trapped atoms. In our setup, the intensities of the beams in each pair are carefully balanced, yielding in principle a centrosymmetric situation. Note however that small defects are always present in the spatial profiles of the beams, creating a local intensity imbalance which can possibly affect the details of the cloud's dynamics.

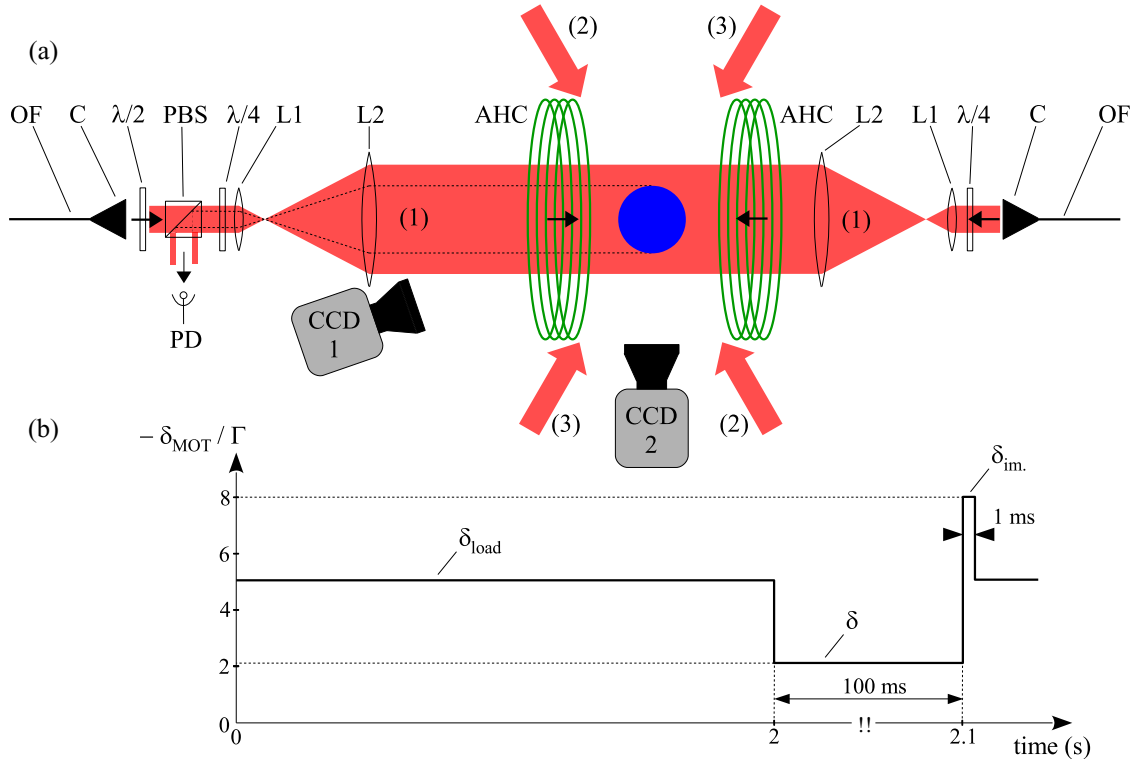[*]To whom correspondence should be addressed: guillaume.labeyrie@inphyni.cnrs.fr

FIG. 1. Experimental procedure. (a) Details of the arrangement for one pair of MOT beams (1). The other two pairs [(2) and (3)] are identical and orthogonal to the first one. The beams are delivered by polarization-maintaining single-mode optical fibers (OF) coupled to a collimator (C). The beams intensities are balanced using a half-wave plate ($\lambda/2$) and polarizing beam splitter (PBS) assembly placed on one arm. The PBS also allows us to collect part of the counterpropagating beam after its passage through the cloud, for optical density measurement using a photodiode (PD). The beams are expanded to a waist of 3.4 cm using afocal telescopes ($L_1 + L_2$). Their polarization is adjusted using quarter-wave plates ($\lambda/4$). The magnetic field gradient is provided by a pair of anti-Helmoltz coils (AHC). (b) Timing of the experiment. The MOT is loaded for 2 s with a detuning δ_{load}, adjusted to maintain the number of atoms fixed during the measurement. The detuning is then changed to δ for 100 ms (instability phase). An image is finally acquired with a fixed detuning $\delta_{im.} = -8\Gamma$.

The peak intensity for each beam is $I = 5$ mW/cm^2. The corresponding saturation parameter per beam is $s = \frac{I/I_{\text{sat}}}{1+4(\delta/\Gamma)^2} \approx 0.08$ for $\delta = -3\Gamma$, assuming atoms are pumped into the stretched Zeeman substates ($I_{\text{sat}} = 1.67$ mW/cm^2). Γ is the natural line width of the transition ($\frac{\Gamma}{2\pi} = 6.06$ MHz). In addition to the trapping light, all beams also contain a small amount of "repumping" light tuned close to the $F = 1 \rightarrow F' = 2$ transition to maintain the atoms in interaction with the trapping laser beams.

The magnetic field gradient required for atom trapping is generated by a pair of coils in anti-Helmoltz configuration. It is anisotropic, twice stronger along the coil's axis than in the transverse plane. Three pairs of Helmoltz coils are also used to compensate for stray magnetic fields at the position of MOT center. Because of this, the position of the cloud in the stable regime does not vary in the course of the experiment when the magnetic field gradient is adjusted.

In Sec. IV we will present the measured threshold detunings as the magnetic field gradient is varied, while keeping the number of trapped atoms N fixed. Since we employ a vapor-loaded MOT where the steady-state value of N is determined by $(\delta, \nabla B)$, this requires us to use the temporal sequence of Fig. 1(b). It is composed of three successive phases that are continuously cycled. In the first phase, we load the MOT for a duration of 2 s with a detuning δ_{load}. We set the value of N by adjusting δ_{load}. We then, in the second phase, rapidly change the detuning for 100 ms to a value δ, which determines the dynamical regime of the MOT that we wish to probe. Finally, in the third phase, the detuning is adjusted to $\delta_{\text{im.}} = -8\,\Gamma$ for 1 ms to perform a fluorescence image acquisition.

We can image the cloud from two directions at 90°, giving access to projections of the atomic distribution along the three spatial dimensions. However, in the following we will only present data obtained with CCD 1 (see Fig. 1). Note that the assumption that the detected fluorescence is proportional to the column density is safe because of the large detuning chosen for the imaging [17]. An absorption imaging scheme, not represented in Fig. 1, allows us to determine the value of N.

The measurement sequence of Fig. 1(b) enables us to maintain a fixed atom number determined by δ_{load}. The 100 ms delay between detuning step and image acquisition is necessary to decorrelate the observed dynamics from the "kick" applied to the atoms as the detuning is abruptly changed. Note however that this delay is small compared to the loading time constant of the MOT (≈ 2 s), which ensures that the atom number is determined by δ_{load} and remains approximately independent of $\delta_{\text{inst.}}$. Since only one image is recorded for each

sequence, by cycling over many runs (typically a hundred) we randomly probe the dynamics.

III. PREVIOUS THEORETICAL APPROACHES AND THREE-DIMENSIONAL NUMERICAL SIMULATIONS

A. Previous theoretical approaches

We briefly recall here the evolution of the theoretical approaches that were employed in the past to describe the physics of large balanced MOTs. This evolution ultimately led to the development of the three-dimensional numerical approach described in Sec. III B.

The model introduced in the 1990s by Wieman and co-workers [3] was the first to describe the operation of the MOT in the stable, multiple-scattering regime. It relies on a Doppler description of the trapping forces which seems appropriate for very large MOTs, although it is known that sub-Doppler mechanisms can play an important role for alkali MOTs at low and moderate atom numbers [2,18].

Contrary to the case of small atom numbers, where the dynamics is governed by single-atom physics and the MOT size is determined by the temperature of the gas, in the regime of large atom numbers the radiation pressure forces acting on the atoms depend on the atomic density distribution and can therefore lead to collective behavior. This occurs when the optical density of the cloud at the trapping laser frequency becomes non-negligible. On one hand, the trapping beams are then attenuated while propagating through the cloud, which produces a density dependent compression force [14]. On the other hand, the scattered photons can be rescattered by other atoms, resulting in a Coulomb-like repulsion force [3]. Because the absorption cross section for scattered photons σ_R is different from and larger than that for laser photons σ_L, the repulsion force is larger than the compression force and the cloud expands when N is increased [3,19]. At equilibrium, the atomic density inside the cloud is constant and only determined by the ratio $\frac{\sigma_R}{\sigma_L}$, and does not depend on N. This results in a characteristic $R \propto N^{1/3}$ scaling law [3,17], providing a clear signature of this regime defined by a spatially linear trapping force and weak attenuation of the trapping beams.

This simplified treatment of [3] was extended in [9] in order to account for larger optical densities and to analyze MOT instabilities that can occur for larger atom numbers. This approach allowed us to derive a criterion for the threshold of MOT instabilities that were observed when N exceeded a certain critical value. In this model, which assumed a constant density, the nonlinear dependence of the attenuated trapping force on both position and velocity was retained. An unstable regime was found to occur when the cloud's radius was larger than a critical value R_c given by

$$\mu \, \nabla B \, R_c \approx |\delta|, \tag{1}$$

where $\mu = 2\pi \times 1.4 \times 10^6 \ \text{s}^{-1} \, \text{G}^{-1}$ for the considered rubidium transition. The MOT thus becomes unstable when the Zeeman detuning at the cloud's edge exceeds the absolute value of the laser detuning. In this situation, the total force at the cloud's edge reverses its sign, and the atomic motion becomes driven instead of damped. For $\delta = -2\Gamma$ and $\nabla B = 10$ G/cm, the criterion given by Eq. (1) yields $R_c \approx 9$ mm.

Such a large MOT size typically requires a large atom number $N > 10^{10}$. While this simplified model provided an intuitive picture for the emergence of the instability and the existence of an instability threshold, it did not make quantitative predictions and was not able to describe the dynamics of the unstable cloud.

The assumption of a constant density was relaxed in [20,21], based on a kinetic theory that described the phase space density of the atoms using a spatial radial symmetry hypothesis. The numerical test-particle simulations of the derived kinetic equations were able to confirm the simple instability criterion given by Eq. (1). They also yielded a generic shape for the atomic density distribution of stable clouds under the form of truncated Gaussians. Finally, these simulations provided insights on the mechanism of the instability, and gave access to the dynamics of the cloud in the unstable regime. However, a limitation of this approach was the assumed spherical symmetry, effectively reducing the dimension of the problem to 1D and preventing, e.g., center-of-mass motion in the dynamics of the unstable cloud.

B. Three-dimensional numerical simulations

To overcome the limitations of the previous models, we have developed a three-dimensional (3D) numerical approach based on a microscopic description of the light-atom interaction. One of the motivations to attempt simulating the full three-dimensional dynamics of the cloud is the intrinsically anisotropic nature of the trap due to the magnetic field gradient. The detailed description of this model will be published elsewhere, we simply outline here its main features.

Since modeling 10^{11} atoms is out of reach with present computers, we used $N_s = 7 \times 10^3$ "superparticles," each representing $\alpha = \frac{N}{N_s}$ real atoms. The mass and scattering cross section of these superparticles are α times larger than that of individual atoms. We checked the validity of this approach by verifying that the outcome of the simulation becomes independent of N_s for $N_s > 5 \times 10^3$. What we simulate is the dynamics of these N_s particles submitted to the three MOT forces mentioned earlier: the trapping force, the compressive attenuation force, and the repulsive rescattering force. The finite temperature of the cloud is accounted for by including a velocity diffusion term in the dynamics, which depends on the photon scattering rate for each particle. We use a leap-frog algorithm [22] to compute the particles dynamics.

In the following we describe the essential steps employed in the simulations. We use a Doppler model for the various forces, which are based on radiation pressure. To simplify the expressions given below, we assume here that our particles are two-level atoms. However, in the simulation we use a more realistic $0 \to 1$ transition model. It is obviously much simpler than the actual $2 \to 3$ transition of the $D2$ line of ^{87}Rb used in the experiment, but allows for a correct description of the three-dimensional trapping by the MOT including the anisotropic magnetic field gradient [23]. Since inelastic photon scattering plays an essential role in the widely accepted MOT description of [3], we include saturation effects to the lowest order both in the scattering cross sections and by including inelastic scattering. However, we neglect higher-order effects such as discussed in [24].

To calculate the forces acting on a particle located at position r, we first compute the local intensity $I(r)$ of each of the six laser beams. This is achieved by calculating their attenuation due to the rest of the cloud. By summing independently the radiation pressure forces F_{rp} due to each beam, we obtain the trapping plus attenuation force.

The radiation pressure exerted by one laser beam of intensity $I(r)$ on an atom located at position **r** is of the form

$$F_{rp}(r, v) = \frac{\sigma_L(r, v)I(r)}{c}, \tag{2}$$

where c is the speed of light. The scattering cross section for a laser photon σ_L is

$$\sigma_L(r, v) = \frac{3\lambda^2}{2\pi} \frac{1}{1 + I_{\text{tot}}(r)/I_s + [2\delta_{\text{eff}}(r, v)/\Gamma]^2}, \tag{3}$$

where λ is the wavelength of the atomic transition. The presence of the other laser beams is taken into account by the $I_{\text{tot}}(r)$ term in the denominator of expression (3), which is the total local laser intensity obtained by summing the intensities $I_i(r)$ of each laser beam.

Considering for simplification a beam propagating in the positive x direction, the Doppler- and Zeeman-shifted detuning δ_{eff} is

$$\delta_{\text{eff}}(x, v) = \delta - \mathbf{k} \cdot \mathbf{v} - \mu \nabla Bx. \tag{4}$$

The rescattering force acting on the particle at position r is obtained by summing all binary interactions with the other particles in the cloud. For a second particle located at position r', the binary interaction $F_{\text{bin}}(r, r')$ is of the form

$$F_{\text{bin}}(r, r') = \frac{I_{\text{tot}}(r')\sigma_L(r')\sigma_R(r, r')}{4\pi c(r' - r)^2}. \tag{5}$$

The computation of the reabsorption cross-section σ_R is not straightforward. It involves the convolution of two quantities: the absorption cross section for a scattered photon with a certain frequency by the atom illuminated by the total laser field of intensity $I_{\text{tot}}(r)$, and the spectrum of the light scattered by the atom at position r' [3,25]. Indeed, the atom is a nonlinear scatterer for light, and the scattering process is inelastic if the saturation parameter is not negligible compared to unity. We compute both the scattered light spectrum and the absorption cross section for scattered light using the approach developed by Mollow [26,27]. Note that since we take into account the inhomogeneous laser intensity distribution inside the cloud, σ_R depends on both spatial coordinates r and r', and thus plays the role of a nonlocal effective charge in the Coulombian binary interaction described by Eq. (5).

An illustration of the result of this simulation is provided in Fig. 2, where we plot the cloud's *rms* radius versus the number of simulated atoms, in the stable regime. As can be observed, below 10^7 atoms the cloud size is N independent and its profile is Gaussian as expected in the temperature-limited regime. For $N > 10^8$, the cloud's radius increases as $N^{1/3}$ (dashed line), the scaling predicted by Ref. [3]. The increase of cloud size with N is a clear signature of the multiple-scattering regime. Within this regime, we observe variations of the cloud's density profile. Around 10^9 atoms, the profile displays a rather flat top. At even higher atom numbers, the top of the profiles rounds off and gets closer to a
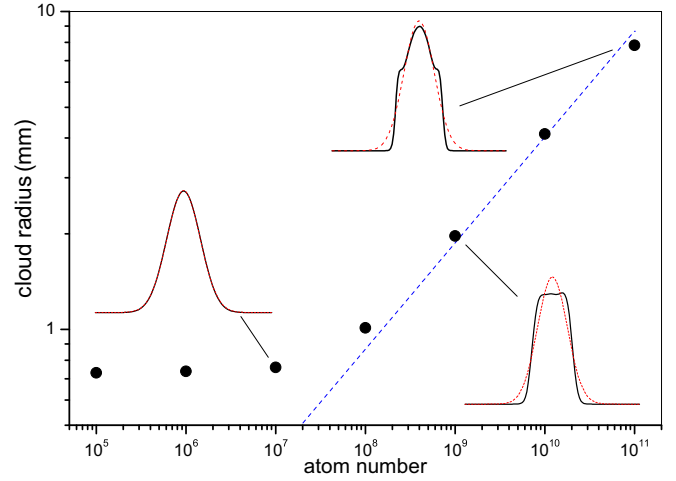

FIG. 2. Simulated MOT size versus N. The parameters are $\delta = -5.5\Gamma$, $\nabla B = 7.2$ G/cm, and $I = 5$ mW/cm². We plot the cloud's rms radius versus N (dots). The dashed line corresponds to the $N^{1/3}$ scaling. The insets show examples of cloud density profiles which have been spatially rescaled. The solid curves are the density profiles while the dashed curves correspond to Gaussian fits.

Gaussian. In all instances, however, the wings of the profiles in the multiple-scattering regime are decaying faster than a Gaussian. Overall, the observed evolution is consistent with our previous observations [17], and also with the theoretical predictions of Ref. [20]. It should be noted that the simulated clouds are systematically larger than those observed in the experiment, roughly by a factor 2. We discuss the implications of this observation in Sec. V.

The numerical simulations not only reproduce the behavior of a stable MOT in the multiple scattering regime, but also and most importantly they yield an unstable behavior for parameters close to those used in the experiments. The onset of the instability as observed in the simulations is illustrated in Fig. 3. We observe a sharp transition between stable and unstable behaviors when the control parameter, here is the laser detuning, is varied. We plot the temporal evolution of the rms radius of the cloud both below ($\delta = -3\Gamma$) and above ($\delta = -2.8\Gamma$) threshold. The initial transient (first 50 ms) is due to the slight mismatch in size and shape between the Gaussian atomic distribution used as a starting point for the simulation, and the final distribution. In the unstable regime, we generally observe another transient before the onset of oscillations, whose duration depends on the distance from threshold. In Fig. 3 this duration is roughly 0.4 s.

IV. EXPERIMENTAL RESULTS AND COMPARISON WITH SIMULATIONS

A. Experimental determination of instability threshold

To determine the instability threshold, we monitor the evolution of the cloud's spatial density distribution during the dynamics. As discussed in Sec. II, only one image is recorded during each experimental cycle described in Fig. 1(b), which corresponds to a random probing of the dynamics of the cloud. We thus record a given set of typically 50 images, and then compare the images two by two. This is done
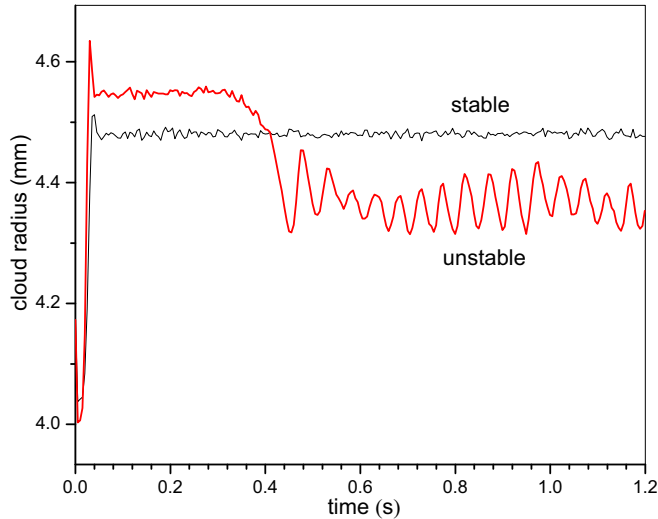
FIG. 3. Instability of simulated MOT. We plot the cloud's rms radius versus time, in the stable regime ($\delta = -3.0\Gamma$, thin curve) and in the unstable regime ($\delta = -2.8\Gamma$, bold curve). The parameters are: $N = 1.5 \times 10^{10}$, $\nabla B = 3$ G/cm, and $I = 5$ mW/cm^2.

by subtracting the two images, and spatially integrating the squared difference image. After normalization, this operation yields the "cloud fluctuation" of Fig. 4, a number whose value is zero if the two images are identical, and one if there is no overlap between the two density distributions (corresponding to a maximal deformation). The operation is repeated for many pairs of images and the corresponding fluctuations are averaged.

Figure 4 illustrates the behavior of the cloud fluctuation as δ is varied over the whole experimental range $-4\Gamma \leqslant \delta \leqslant -0.8\Gamma$, for the three values of ∇B. As can be seen, crossing
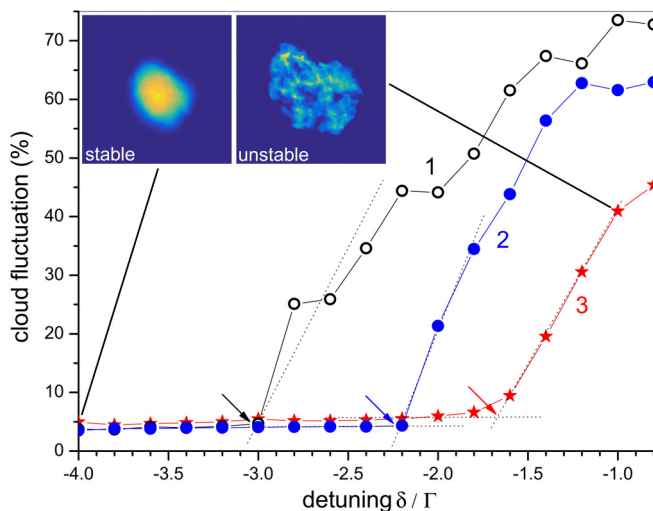

FIG. 4. Determination of instability threshold. We plot the cloud fluctuation (see text) versus detuning for three values of magnetic field gradient: (1) $\nabla B = 12$ G/cm (open circles), (2) $\nabla B = 4.8$ G/cm (dots), and (3) $\nabla B = 1.2$ G/cm (stars). An extrapolation of the observed growth rate (dotted lines) allows us to determine the threshold detuning (arrows). The insets show examples of fluorescence images for a stable and an unstable cloud.
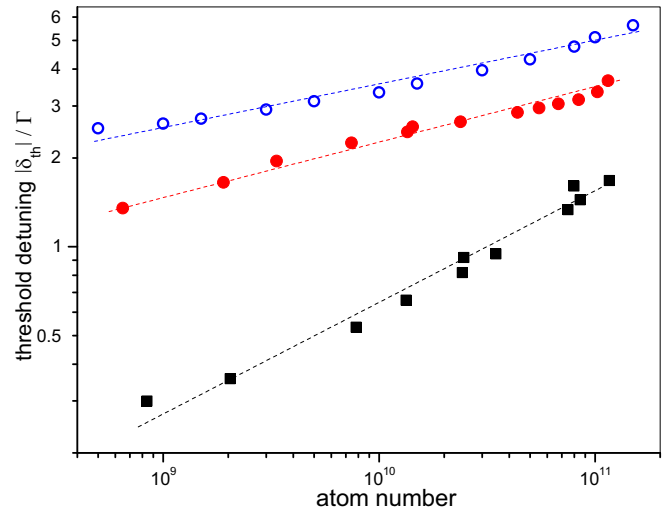

FIG. 5. Threshold detuning (absolute value) versus atom number. The dots are experimental data for a magnetic field gradient $\nabla B = 7.2$ G/cm and a beam intensity $I = 5$ mW/cm^2. The circles are the simulation result for the same parameters. The squares correspond to the prediction of the model of Ref. [9] using experimentally measured cloud sizes (see text). The dotted lines correspond to linear fits of the log-log data.

the threshold results in an abrupt increase of the fluctuation. The position of the threshold can be estimated by fitting the initial growth by a linear function and extrapolating to the value below threshold.

B. Threshold detuning versus atom number

In this section we study the impact of N on the instability threshold. To this end we vary the number of trapped atoms by adjusting the diameter of the MOT beams using diaphragms. This provides an efficient way of tuning N without affecting the other MOT parameters, as demonstrated in [17].

The experimental variation of δ_{th} with N is reported in Fig. 5 (dots), in log-log scale. Very roughly, we observe that $|\delta_{th}|$ increases by Γ when N increases by one order of magnitude. A linear fit of the data in the log-log plot yields a slope of 0.17 (dotted line). The result of the numerical simulations described in Sec. III B is reported in circles. It shows a similar scaling, but with an offset of approximately Γ.

We also show the prediction of the model of Ref. [9] (squares), as given by Eq. (1). This equation establishes a link between ∇B, δ, and the critical radius R_c, but does not provide an expression for the cloud size as a function of N. Thus we use the cloud sizes measured in the experiment to compute δ_{th} using Eq. (1). However, the model of [9] assumes a constant density while the experimental profiles are closer to Gaussians. We thus have to choose a definition of R_c to use in Eq. (1). In Fig. 5 we used $R_c = 2\sigma$, where σ is the measured rms cloud size in the plane of the magnetic field gradient coils. Since we find a scaling $\sigma \propto N^{0.36}$, the prediction Eq. (1) is definitely different from both the experimental observation and the result of the numerical simulations. This is a clear indication that the model used in [9] cannot quantitatively
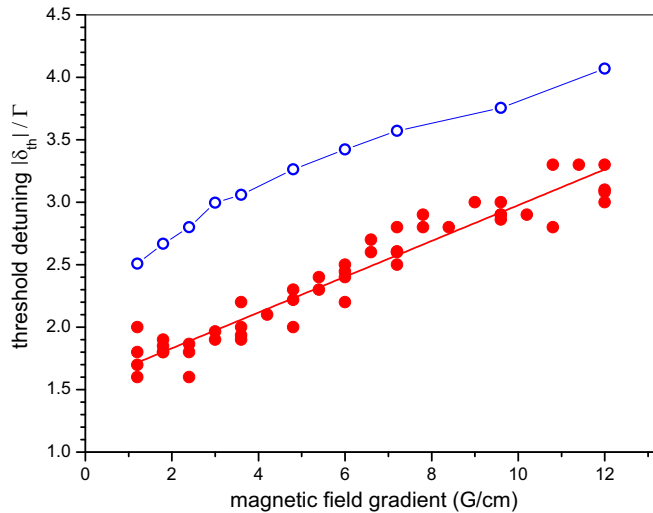
FIG. 6. Threshold detuning versus magnetic field gradient at fixed atom number. The experimental data (including several runs) is shown as dots, with a linear fit (solid line). The parameters are $N = 1.5 \times 10^{10}$ and $I = 5$ mW/cm^2. The circles correspond to the numerical simulation result.

describe the dependence of the instability threshold on the atom number.

C. Threshold detuning versus magnetic field gradient at fixed atom number

We now present measurements of the threshold detuning δ_{th} as ∇B is varied, using the procedure described in Sec. II to maintain a fixed number of trapped atoms $N = 1.5 \times 10^{10}$. The results of different experimental runs are shown as dots in Fig. 6, together with a linear fit taking into account all the data (solid line). The threshold detuning is seen to increase (in absolute value) linearly with ∇B, with a slope $\approx 0.14\Gamma$ (G/cm).

We compare the experimental data to the result of the numerical simulations (circles) using the experimental parameters. Once again we observe that the slopes of both experimental and simulated curves are very similar. This agreement is a good indication that our numerical model captures efficiently the main ingredient involved in the determination of the instability threshold. We note again that the simulated thresholds are systematically larger (in absolute value) than the experimental ones by approximately Γ.

V. DISCUSSION

The new experimental data reported in this work need to be compared to our earlier results of [9]. They are obtained in conditions that are both better controlled (threshold at constant N) and more extended (threshold as a function of N), and thus put more stringent constraints on the models they are being compared to. In particular, the simple analytical model of [9], which seemed in reasonable agreement with the early experimental data, is now clearly unable to reproduce the scaling observed when the atom number is varied. Although we have no reason to question the physical picture of the instability mechanism that it conveys, it is too simplified to reproduce even qualitatively the experimentally observed behavior.

This is not the case for the numerical simulations, which are in good qualitative agreement with both experiments at fixed N and as a function of N. This indicates that our improved model catches the important ingredients determining the behavior of the MOT instability threshold. We plan in the future to investigate which of these ingredients are determinant in describing the correct MOT behavior.

The constant offset of about one Γ in the threshold detuning between experiment and numerics is probably linked to the larger cloud sizes found in the simulations. The origin of this mismatch is not at present clearly identified, but it is not surprising considering the large number of simplifications still included in the model. The most prominent is the simplified atomic structure, possibly yielding a different effective Zeeman shift in the MOT.

VI. CONCLUSION

We presented in this paper a detailed experimental and numerical study of the instability threshold for a balanced, six-independent beams magneto-optical trap containing large numbers of cold atoms. Using an improved experimental scheme, we were able to study the impact of the atom number on the threshold. We also measured the $(\delta, \nabla B)$ unstable boundary while maintaining this atom number fixed. These experimental results were compared to a three-dimensional numerical simulation of the MOT based on a microscopic description. We obtain a good qualitative agreement, despite some unavoidable simplifications in the description of the MOT physics. The scaling of the threshold with atom number, for both experiment and simulations, is clearly different from that given by the analytical approach of [9]. Our numerical model also allows us to go beyond the approach of [20], which was assuming a central symmetry. In particular we now can and do observe center-of-mass as well as radial oscillations. This approach will be useful in the future to investigate the atom cloud dynamics in the unstable regime.

[1] E. L. Raab, M. Prentiss, A. Cable, S. Chu, and D. E. Pritchard, Trapping of Neutral Sodium Atoms with Radiation Pressure, Phys. Rev. Lett. **59**, 2631 (1987).

[2] J. Dalibard and C. Cohen-Tannoudji, Laser cooling below the Doppler limit by polarization gradients: simple theoretical models, J. Opt. Soc. Am. B **6**, 2023 (1989).

[3] T. Walker, D. Sesko, and C. Wieman, Collective behavior of Optically Trapped Neutral Atoms, Phys. Rev. Lett. **64**, 408 (1990).

[4] J. T. Mendonça, R. Kaiser, H. Terças, and J. Loureiro, Collective oscillations in ultracold atomic gas, Phys. Rev. A **78**, 013408 (2008).

[5] J. D. Rodrigues, J. A. Rodrigues, A. V. Ferreira, and J. T. Mendonça, Collective processes in a large atomic laser cooling experiment, Opt. Quant. Electron. **48**, 169 (2016).

[6] J. Barré, R. Kaiser, G. Labeyrie, B. Marcos, and D. Métivier, Towards a measurement of the Debye length in very large magneto-optical traps, Phys. Rev. A **100**, 013624 (2019).

[7] J.-P. Hansen, I. R. McDonald, and E. L. Pollock, Statistical mechanics of dense ionized matter. III. Dynamical properties of the classical one-component plasma, Phys. Rev. A **11**, 1025 (1975).

[8] M. P. Evrard *et al.*, Drift waves, anomalous diffusion and equilibrium in a magnetized plasma column, Plasma Phys. **21**, 999 (1979).

[9] G. Labeyrie, F. Michaud, and R. Kaiser, Self-Sustained Oscillation in a Large Cloud of Cold Atoms, Phys. Rev. Lett. **96**, 023003 (2006).

[10] J. P. Cox, *Theory of Stellar Pulsation* (Princeton University Press, Princeton, NJ, 1980).

[11] D. Wilkowski, J. Ringot, D. Hennequin, and J. C. Garreau, Instabilities in a Magneto-Optical Trap: Noise-Induced Dynamics in an Atomic System, Phys. Rev. Lett. **85**, 1839 (2000).

[12] A. di Stephano, P. Verkerk, and D. Hennequin, Deterministic instabilities in the magneto-optical trap, Eur. Phys. J. D **30**, 243 (2004).

[13] J. T. Mendonca and R. Kaiser, Photon Bubbles in Ultracold Matter, Phys. Rev. Lett **108**, 033001 (2012).

[14] J. Dalibard, Laser cooling of an optically thick gas: The simplest radiation pressure trap? Opt. Commun. **68**, 203 (1988).

[15] A. di Stefano, M. Fauquembergue, P. Verkerk, and D. Hennequin, Giant oscillations in a magneto-optical trap, Phys. Rev. A **67**, 033404 (2003).

[16] R. Romain, A. Jallageas, P. Verkerk, and D. Hennequin, Spatial instabilities in a cloud of cold atoms, Phys. Rev. E **94**, 052212 (2016).

[17] A. Camara, R. Kaiser, and G. Labeyrie, Behavior of a very large magneto-optical trap, Phys. Rev. A **90**, 063404 (2014).

[18] K. Kim, H.-R. Noh, H.-J. Ha, and W. Jhe, Direct observation of the sub-Doppler trap in a parametrically driven magneto-optical trap, Phys. Rev. A **69**, 033406 (2004).

[19] A. M. Steane, M. Chowdhury, and C. J. Foot, Radiation force in the magneto-optical trap, J. Opt. Soc. Am. B **9**, 2142 (1992).

[20] T. Pohl, G. Labeyrie, and R. Kaiser, Self-driven nonlinear dynamics in magneto-optical traps, Phys. Rev. A **74**, 023409 (2006).

[21] G.-L. Gattobigio, T. Pohl, G. Labeyrie, and R. Kaiser, Scaling laws for large magneto-optical traps, Phys. Scr. **81**, 025301 (2010).

[22] C. Y. Kaya and L. Noakes, in *The Leapfrog Algorithm: Background and Demonstration*, edited by L. Caccetta, K. L. Teo, P. F. Siew, Y. H. Leung, L. S. Jennings, and V. Rehbock, Proceedings of the International Conference on Optimization Techniques and Applications (Curtin University, Perth, 1998), Vol. 1, pp. 835–842.

[23] K. A. Brickman, M. S. Chang, M. Acton, A. Chew, D. Matsukevich, P. C. Haljan, V. S. Bagnato, and C. Monroe, Magneto-optical trapping of cadmium, Phys. Rev. A **76**, 043411 (2007).

[24] R. Romain, D. Hennequin, and P. Verkerk, Phase-space description of the magneto-optical trap, Eur. Phys. J. D **61**, 171 (2011).

[25] L. Pruvost, I. Serre, H. T. Duong, and J. Jortner, Expansion and cooling of a bright rubidium three-dimensional optical molasses, Phys. Rev. A **61**, 053408 (2000).

[26] B. R. Mollow, Power spectrum of light scattered by two-level systems, Phys. Rev. **188**, 1969 (1969).

[27] B. R. Mollow, Stimulated emission and absorption near resonance for driven systems, Phys. Rev. A **5**, 2217 (1972).